Inclusive proton production cross sections in (d,xp) reactions induced by 100 MeV deuterons

D. Ridikas,* W. Mittig, H. Savajols, and P. Roussel-Chomaz
GANIL, BP 5027, F-14076 CAEN Cedex 5, France

S. V. Förtsch, J. J. Lawrie, and G. F. Steyn
NAC, P.O. Box 72, 7131 Faure, South Africa

(Received 24 June 2000; published 20 December 2000)

Energy spectra and angular distributions of protons emitted from the inclusive (d,xp) reaction on ^{9}Be, ^{12}C, ^{27}Al, ^{58}Ni, ^{93}Nb, ^{181}Ta, ^{208}Pb, and ^{238}U were measured at an incident deuteron energy of 100 MeV. The protons were detected at laboratory scattering angles of 6° to 120° and 8° to 120° for the targets with $9 \leqslant A \leqslant 27$ and $A \geqslant 58$, respectively. Two triple-element and three double-element detector telescopes allowed for a low energy detection threshold of 4 to 8 MeV. The experimental results are presented in double-differential as well as angle- and energy-integrated cross sections. For all the nuclei studied, the energy spectra at forward angles show pronounced deuteron breakup peaks centered around approximately half of the incident deuteron energy. Qualitatively the energy spectra are similar for all nuclei at a given angle except in the region of the low-energy evaporation peak. As a function of target mass the evaporation cross sections are found to increase up to $A=58$ after which they decrease again. The total preequilibrium proton cross section is roughly $(280 \pm 60)A^{1/3}$ mb. The angular distributions at the high emission energies are strongly forward peaked while the distributions of the low-energy protons are almost isotropic. The LAHET code system (LCS) was applied to calculate the proton production cross sections. Standard LCS calculations are found to underpredict the experimental cross sections at the very forward angles on the heavy target nuclei ($A \gtrsim 58$). By adding incoherently the Coulomb breakup cross section of the deuteron to the LCS calculations the experimental cross sections are reproduced to within 10%. Although preequilibrium processes are a necessary ingredient in the LCS calculations of the large-angle cross sections, this code still fails to predict the experimental evaporation distributions.

DOI: 10.1103/PhysRevC.63.014610 PACS number(s): 24.10.−i, 25.10.+s, 25.60.Dz

I. INTRODUCTION

The increasing demand for powerful neutron sources is leading to a renewed interest in neutron production reactions. One of the most studied reactions in this regard is the spallation reaction whereby an energetic particle striking a heavy target nucleus causes the emission of tens of neutrons. However, the most efficient way of converting the initial beam energy into neutron production, still remains one of the crucial problems in the efficient operation of accelerator driven systems (ADS), e.g., in subcritical hybrid systems [1].

So far only proton-induced reactions at medium energies (0.8–1.6 GeV) on heavy targets were considered in ADS's to provide intense neutron spallation sources [2–4]. Consequently, both theoretical models and experimental data have been further extended mainly for proton-induced reactions. The theoretical model most often employed to describe these reactions is the intranuclear cascade (INC) model [5–7], which is in fact a combination of several other models, each corresponding to a specific stage in the time evolution of the reaction. Roughly, these processes can be viewed as proceeding in two stages [8]: (a) in the first (fast) stage the incident particle loses part of its energy by individual nucleon-nucleon collisions; (b) in the second (slow) stage target excitation energy is released by evaporation.

However, the use of other projectiles such as deuterons to produce fast neutrons has been studied since the 1940's [9]. This alternative process to proton-induced neutron production is certainly regarded to be competitive, if not even more efficient as reported in Ref. [10]. Recently, a brief survey of nucleon production calculations for deuteron induced reactions in the 100–1200 MeV range was presented [10,11]. These authors have shown that a characteristic narrow peak in the energy distribution for large nucleon emission energies, seen clearly at forward angles and for heavy metal targets, is not properly reproduced by the conventional codes [12,13] employed in the simulations of the ADS [14,15]. It was suggested that in the deuteron-induced reaction, the coherent Coulomb dissociation of the incident deuteron was not taken into account properly, and that this process enhances the high energy nucleon yield at very forward angles [11]. By adding incoherently the Coulomb dissociation cross section [16] to that calculated using the standard INC routines [12], excellent agreement with the absolute values of the available data was obtained over the entire energy region of the emitted nucleons [11]. To confirm these predictions and to clarify under which conditions the Coulomb dissociation process is important for calculations of the total nucleon production, good quality forward angle data are required. The Coulomb dissociation cross section increases with decrease in energy, therefore its relative contribution to the total nucleon production increases Ref. [11]. The lack of such experimental data at the low incident deuteron energies in the study of Ref. [11] prompted the present measurements

*Present address: CEA Saclay, F-91191 Gif-sur-Yvette Cedex, France.

at an incident deuteron energy of 100 MeV and at emission angles as far forward as experimentally possible.

Although the main interest for ADS is related to neutron production and neutron applications, we believe that (d,xp) reactions are as useful as (d,xn) reactions in order to investigate the deuteron breakup mechanism. Experimentally, the breakup protons are much easier to measure than the breakup neutrons.

In this work, we have measured complete proton energy spectra for 100 MeV deuterons on eight different target nuclei ranging from $A=9$ to $A=238$. Our main objectives with these measurements are the following.

(1) To extend already existing data on proton production with deuterons (see, e.g., Ref. [17]) to more forward scattering angles and to lighter target nuclei.

(2) To investigate the proton production yield as a function of target mass and the way in which the reaction cross section is distributed over the relevant reaction channels.

(3) To check if the Coulomb dissociation term [11,16] for the direct breakup of the deuteron is taken into account properly in the LAHET code system (LCS) [12] when applied at a lower incident energy.

(4) To test the validity of the LCS [12] for proton production from deuteron induced reactions at an incident energy of 100 MeV, where the basic assumption (independent particle model) of the INC breaks down.

(5) To provide guidance for further theoretical development.

The paper is structured as follows. In Sec. II we describe the experimental method. Section III outlines the data taking and data analysis. Section IV presents the experimental results and discussion. In Sec. V the experimental data are compared with LCS model calculations. The results and their interpretations are summarized in Sec. VI.

II. EXPERIMENTAL METHOD

The experiment was performed at the cyclotron facility of the National Accelerator Center (South Africa) [18]. A detailed layout of the facility can be found in Ref. [19]. The 1.5 m diameter scattering chamber equipped with two rotatable arms was used for this experiment. The deuteron beam was focussed to a spot of 2 mm$\times$2 mm on the target situated at the center of the chamber. The energy of the beam was 99.6 ± 1.0 MeV. Beam halo, which may in principle be a severe problem at forward angles, was monitored on a regular basis during the measurements by comparing the count rates from the target and from an empty target frame. The angular offset of the beam was checked by means of symmetric measurements of elastic cross sections carried out at a selected angle on either side of the beam.

Double differential cross sections of emitted protons were measured with 100 MeV deuterons on eight different target materials. The following targets were used (the number in brackets represents the thickness in mg/cm^2): ^{9}Be(4.7), ^{12}C(1.1), ^{27}Al(5.5), ^{58}Ni(1.1), ^{93}Nb(3.0), ^{181}Ta(3.6), ^{208}Pb(5.7), and ^{238}U(95.0).

The detector assemblies consisted of either double-element or triple-element telescopes, each consisting of a NaI stopping E detector and one or two Si surface barrier ΔE detectors. These assemblies were mounted in the same horizontal reaction plane on the rotating arms of the scattering chamber. An additional compact double-element telescope was used for the measurements at very forward angles.

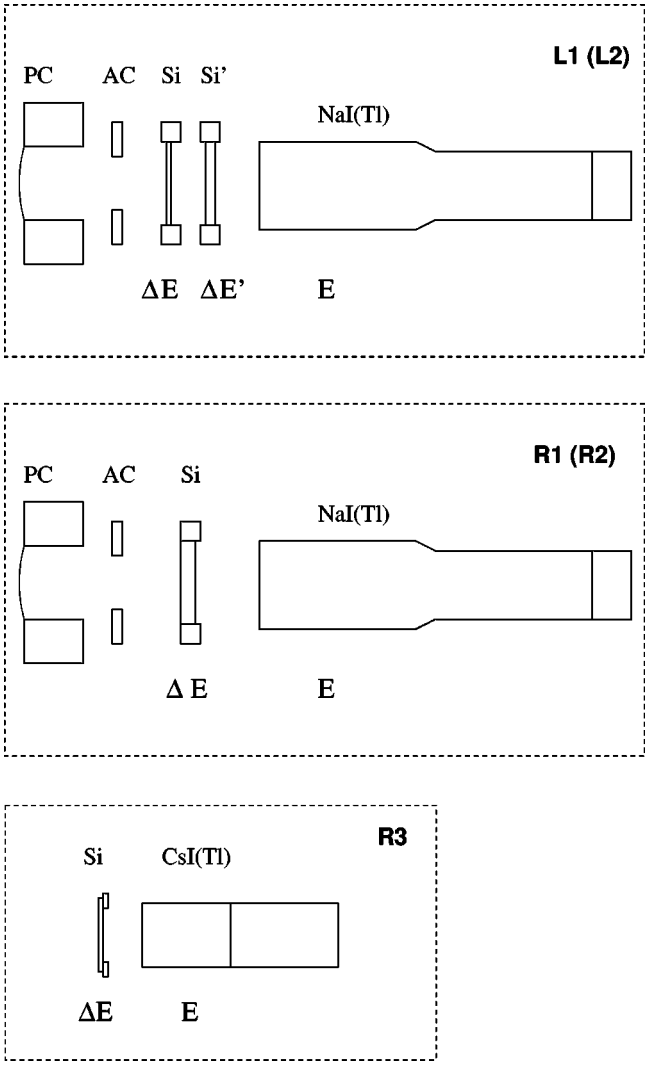

FIG. 1. A detailed presentation of two-element ($R1$, $R2$, and $R3$) and three-element ($L1$ and $L2$) telescopes for charged particle detection. AC stands for active collimator, while PC is for passive collimator.

The double-element telescopes $R1$ and $R2$ as presented in Fig. 1 (500 μm Si detector and 76 mm diameter $\times$127 mm thick NaI) were positioned at angles θ_1 and $\theta_2=\theta_1+10°$, respectively, while the triple-element telescopes $L1$ and $L2$ given in Fig. 1 (100 and 1000 μm Si detectors and 76 mm diameter $\times$127 mm thick NaI) were positioned at the opposite angles $\theta_3=360°-\theta_1$ and $\theta_4=360°-\theta_2$ for symmetrical measurements. The additional compact telescope $R3$ presented in Fig. 1 (300 μm Si detector and 13.5 mm square $\times$80 mm thick CsI) was used at the very forward angles $\theta_5=\theta_1-15°$. Other details of the experimental setup can be found in Refs. [19,14].

Solid brass passive collimators (PC), 15 mm thick with central 16 mm circular holes, were mounted in front of the

TABLE I. Summary of the experimental results for proton production from (d,xp) reactions at $E_d = 100$ MeV.

Target	Low energy cutoff (MeV)	Coulomb barrier V_c (MeV)	Tot. integr. Cross section σ_p (mb)	Evap. Cross section σ_{evap} (mb)	Preequilibr. Cross section σ_p-σ_{evap} (mb)	Proton multiplicity $Y_p = \sigma_p / \sigma_R$
^{9}Be	4	1.25	481	42	439	0.90
^{12}C	4	1.75	610	52	558	1.01
^{27}Al	4	3.12	1308	433	875	1.31
^{58}Ni	4	5.52	2792	1209	1583	1.83
^{93}Nb	4	7.12	2102	836	1266	1.04
^{181}Ta	6	10.53	1658	159	1499	0.55
^{208}Pb	8	11.37	1823	71	1752	0.56
^{238}U	8	12.27	1641	62	1579	0.46

telescopes $L1$, $L2$, $R1$, and $R2$ followed by active collimator assemblies, 6 mm, thick plastic scintillators with central 14 mm circular holes, mounted immediately after the solid brass collimators (see Fig. 1). Consequently, solid angles were defined by the active collimators (AC) in the case of $L1$, $L2$, $R1$, and $R2$ telescopes, while the Si detector was used to define the solid angle of telescope $R3$. The active collimators were used mainly to eliminate slit-scattered events. Kapton foils with a thickness of 8 μm were placed over the front holes of the brass collimators (PC) to reduce the flux of low-energy electrons emitted from the target on the front detectors.

Energy calibrations of the Si detectors were performed with a ^{228}Th α-particle source, whereas the (slightly nonlinear) energy calibration of the NaI and CsI detectors were determined from the kinematics of elastic proton-deuteron scattering from a polyethelene target. Standard fast coincidence electronics and an online data acquisition system were used to process and store the data event-by-event on tape for subsequent offline analysis. A light-emitting diode pulser system allowed for corrections to be made for possible gain drifts in the photomultiplier tubes of the NaI detectors. Corrections for electronic dead time were based on the same pulsers, and computer dead time was automatically corrected by means of a ''busy'' output used as a ''veto'' signal in the electronic equipment and the current integrator. The details of the electronics and computer software are described in Refs. [19,14].

The maximum beam current that could be tolerated, in the range from 0.2 to 20 nA, was determined by the count rates in the telescopes at the forward angles. At the very forward angles ($\theta \leqslant 10°$) even lower beam currents were required, which could not be accurately measured with the current integrator. In this particular case, one of the other double-element telescopes was kept at $\theta_1 = 15°$ to allow for proper normalization by comparing count rates obtained in different runs.

III. DATA TAKING AND DATA ANALYSIS

The double differential proton cross sections were obtained at angles ranging from 30° to 120° in steps of 10°, from 10° to 30° in steps of 5°, at 8° for all eight targets, and at 6° for Be, C, and Al.

Particle identification was achieved in a standard way by generating $\Delta E - \Delta E'$ and $\Delta E' - E$ energy-loss matrices for each detector telescope. This technique permitted unambiguous particle separation over an energy range from a few MeV to the maximum energy which was kinematically allowed. The low-energy threshold (see Table I) is defined mainly by the proton stopping range in the first Si detector and in the target.

The energy spectra were obtained by setting appropriate gates in the particle identification spectra. The total energy spectra were constructed from the sum of the individual signals after energy calibration. Spectra measured at the very forward angles were corrected for the reaction tails produced in the stopping E detector and in some cases for background contributions caused by beam halo.

The largest single contribution to the experimental systematic error is due to the uncertainty introduced by the setting of the gates on the particle identification histogram at the very forward angles ($\theta < 15°$). For the telescopes employed only at forward angles, there was a substantial ''leakage'' of deuteron events into the proton locus, particularly in the region corresponding to the higher particle energies. Deuteron event leakage into this gate is mainly due to the inelastic scattering of deuterons with atoms inside the CsI crystal.

To measure the deuteron reaction tail we have separately performed the $CH_2(d,pd)$ measurements for appropiate kinematic coincidences at forward angles. This allowed for the clear identification of the shape of the tail and the subsequent correction of the proton spectra at forward angles. The subtracted reaction tail contributed up to 25% at 6°–8°, and was less than 1% already at 15°.

Background contributions were measured from an empty target frame and were subtracted accordingly. This contribution to the measured spectrum was always less than 3%, even at the smallest scattering angles measured, i.e., 6°–8°.

Further uncertainties in the absolute cross sections are as follows: (a) The uncertainty of the thicknesses of the targets ($\sim 4\%$). (The target thicknesses were determined by weighing and confirmed by measuring the energy loss of

α particles from ^{228}Th source.) (b) Determination of the solid angles and angular offset of the beam ($\sim 3\%$). This error was obtained from the geometry parameters of the experimental setup and cross-checked by means of the symmetric measurements carried out for each angle on either side of the beam line. (c) The uncertainties due to background corrections ($<5\%$). The biggest uncertainty occurred for the most forward angles; (d) The integrated beam current ($<2\%$ [19]). Other additional uncertainties (incorrect particle identification, the electronics dead time, the target contaminants, etc.) were small ($<2\%$). The angle-integrated total particle production cross section has some uncertainties due to the extrapolation, interpolation, and minimization procedures as discussed below ($<5\%$).

Based on the above mentioned experimental uncertainties, the absolute cross sections are estimated to be accurate to within 10%, except for the lead and uranium targets. In these two particular cases somewhat higher errors are encountered due to additional uncertainties related to the target thickness (U) and target contamination by oxygen (Pb and U) as discussed in more detail in the following section. All corrected spectra were then summed into 2 MeV energy bins.

IV. RESULTS AND DISCUSSION

Double differential laboratory cross sections of the (d,xp) reaction on Be, C, Al, Ni, Nb, Ta, Pb, and U at $E_d = 100$ MeV are displayed in Figs. 2 and 3.[1] Although the measured cross sections all follow a similar trend, the following comments need to be made.

The energy spectra in the case of ^{12}C(d,xp) (upper-right part of Fig. 2) clearly show some discrete peaks which are associated with scattering off hydrogen contamination in the target. These peaks were used as suitable cross checks of the energy calibration since they follow the expected kinematics of the H(d,pd) reaction.

In the case of ^{208}Pb(d,xp) (lower-left part of Fig. 3) the energy spectra, especially at the lower energies should be treated with caution. During the offline data analysis we discovered that the lead target showed signs of oxygen contamination. This can be seen by comparing the low energy spectra for ^{181}Ta(d,xp) and ^{208}Pb(d,xp) as presented by the right-upper part and left-lower part of Fig. 3. At higher energies, $E_p > 16$ MeV, the contribution from oxygen in the proton yield decreases to less than 10%.

As we discovered after the measurements, the energy spectra of ^{238}U(d,xp) (lower-right part of Fig. 3) are severely affected by oxidization of the target. As a result, the change in the target thickness results in uncertainties of up to $\sim 50\%$ in the absolute cross section values.

A. Energy spectra

As shown in Figs. 2 and 3 it can be seen that the magnitude of the high-energy portion of the proton cross sections decreases very rapidly with increasing angles, while the low-energy regions show little variation with angle. At the high-energy ends of the cross sections some discrete structure is seen for all targets at forward angles. These discrete peaks result from deuteron stripping reactions leading to the bound final states of the residual nuclei. The contribution from these states to the total cross section, however, is rather small.

At energies below these high-energy peaks, the cross sections at small angles increase rapidly reaching a maximum at approximately half of the deuteron incident energy. This broad peak is due to the deuteron breakup process which dominates the proton yield at forward angles. The deuteron breakup yield decreases dramatically with increasing angle and the peak location shifts slightly to a lower energy. From Figs. 2 and 3 it can also be seen that the breakup cross section increases with target mass.

Below the deuteron breakup region the cross sections reveal a further maximum at approximately the proton Coulomb barrier energy for each target nucleus. This peak is due to the evaporation of protons. For heavy (Ta, Pb, U) and light (Be, C) nuclei the evaporation peak at forward angles is not as pronounced as in the case of intermediate mass (Al, Ni, Nb) nuclei (see Figs. 2 and 3). First of all, this is due to the fact that the Coulomb barrier attenuates the emission of the low-energy charged particles. Secondly, another two competing processes, namely, neutron evaporation and fission, are more favorable for heavier nuclei. The evaporation peak yield decreases and its peak energy shifts to higher energy with increasing mass. For angles larger than 90° the spectral shapes are very similar and the magnitudes of the peak are almost indepedent of the target mass, indicating that the yield is dominated by the compound nuclear evaporation process. However, as we will discuss later, a small preequilibrium component also appears to exist. From these large-angle spectra the total evaporation cross section is estimated. Both for light (Be, C) and heavy nuclei (Ta, Pb, U), the evaporation process amounts to less than 10% of the total proton yield. In addition to the pronounced deuteron-breakup contribution, underlying preequilibrium processes seem to dominate over the evaporation of protons for these nuclei.

For the medium-mass (Al, Ni, Nb) nuclei, the spectra show pronounced evaporation peaks with significant high-energy cross sections. In this case, the strengths of the evaporation and the preequilibrium processes are comparable.

B. Angular distributions

Typical differential angular distributions of protons for various energy bins are shown in Fig. 4 for the ^{58}Ni(d,xp) reaction. Their overall trend is smooth and is qualitatively similar for all target nuclei studied. The high-energy protons (>20 MeV) show strong forward peaking which suggests that direct or preequilibrium processes dominate the reaction in this region of the cross sections. The distribution of the low-energy protons is nearly isotropic for lighter nuclei and is slightly forward peaked for heavy nuclei.

Since the systematics of continuum angular distributions in nucleon and α-particle induced reactions at energies up to

[1]Numerical values of these cross sections can be obtained from the authors upon request.

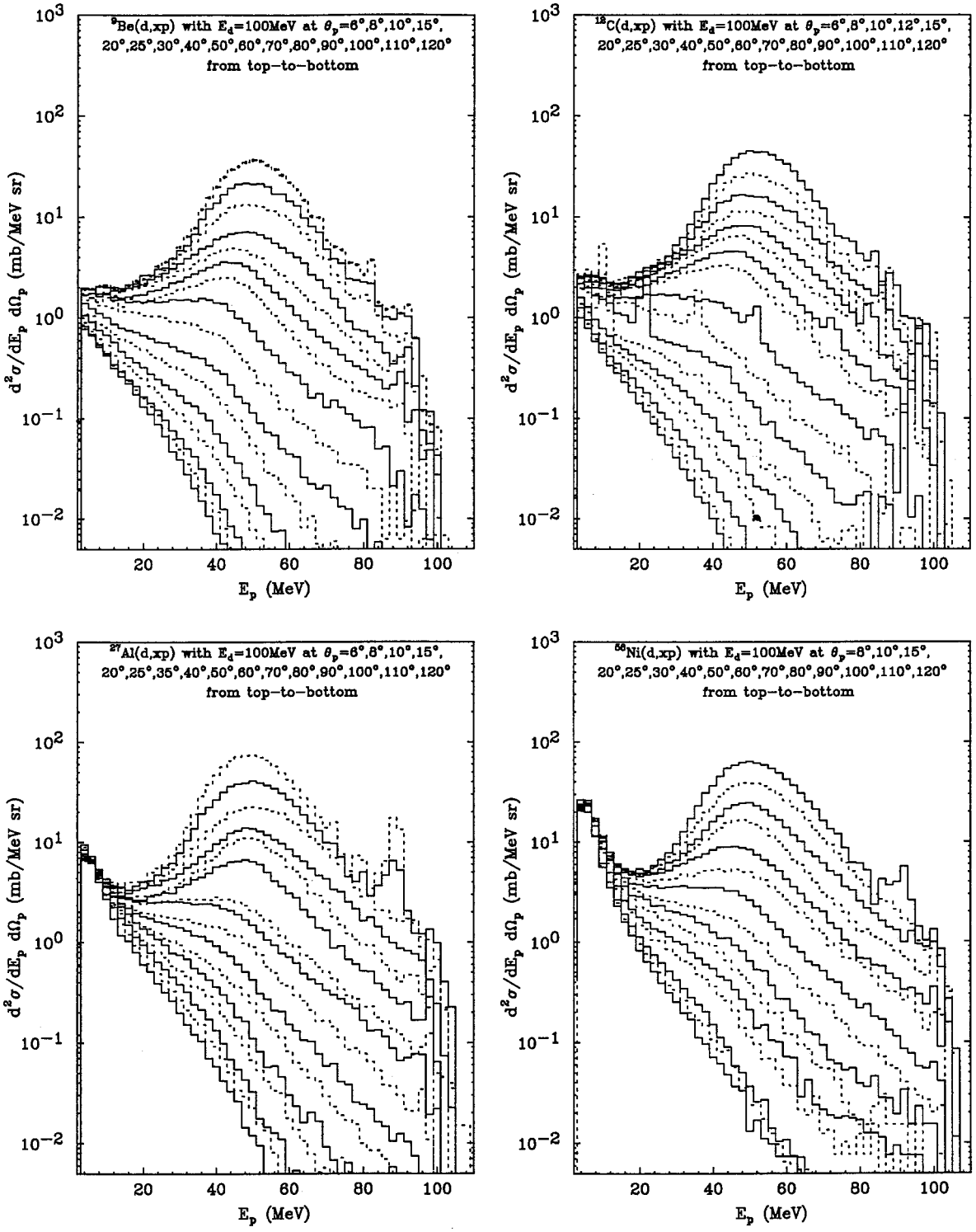

FIG. 2. Double differential cross sections of protons from 6° to 120° with 100 MeV deuterons on ^{9}Be, ^{12}C, ^{27}Al and from 8° to 120° with 100 MeV deuterons on ^{58}Ni.

several hundred MeV have been successfully parametrized by Kalbach-Mann (KM) [21,22], we find it worthwile to examine this phenomenology for deuteron induced reactions.

Briefly, the parametrization of KM consists of a part which accounts for the direct reactions and another which describes the compound-nucleus process [22]. The parametrization is assumed to be related to a multistep direct (MSD) and a multistep compound (MSC) reaction mechanism as the underlying physical processes. The general expression of the KM systematics, for protons ejected with energies E_p and scattering angle θ given in the center-of-mass system, have the following form [22]:

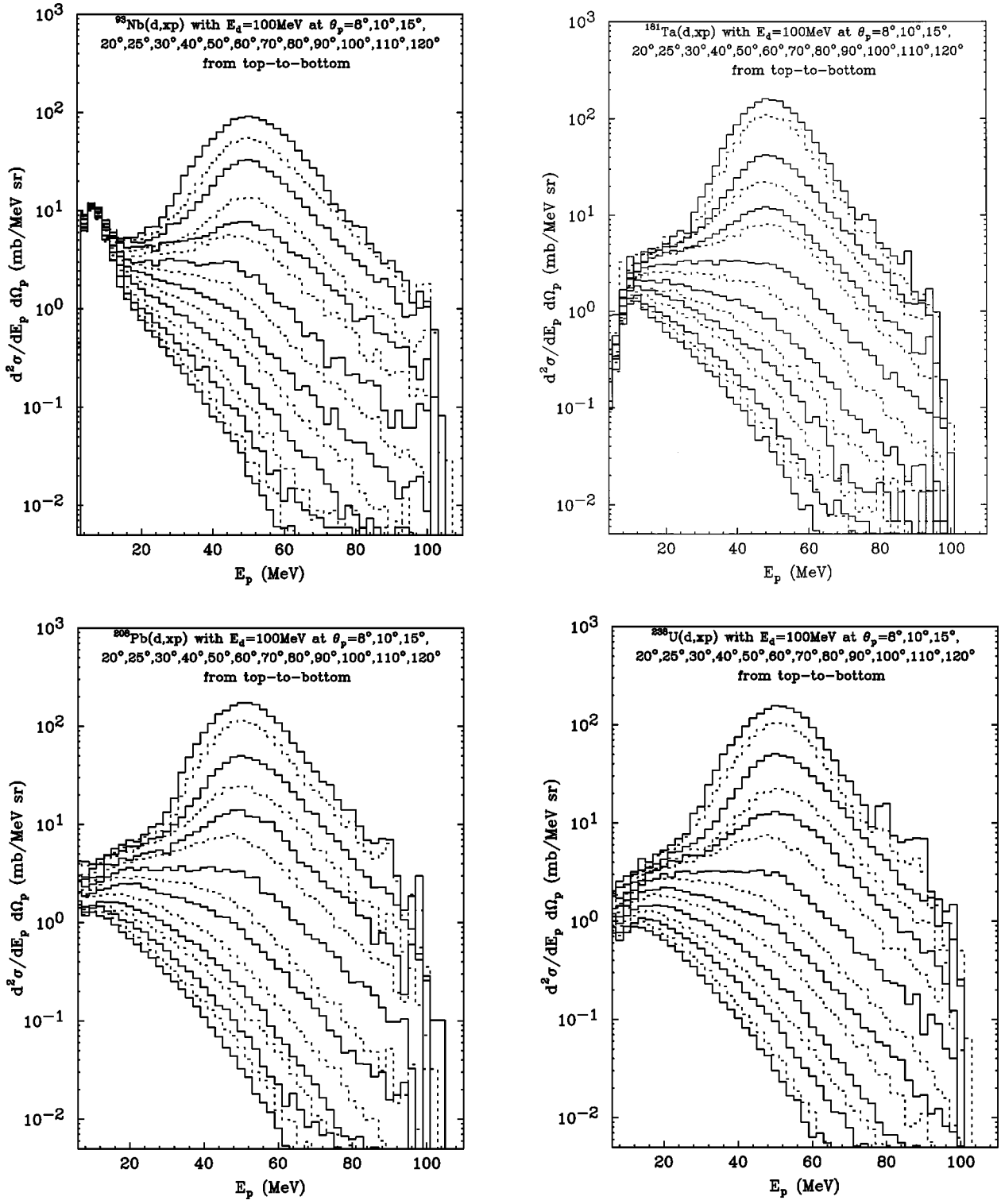

FIG. 3. Double differential cross sections of protons from 8° to 120° with 100 MeV deuterons on ^{93}Nb, ^{181}Ta, ^{208}Pb, and ^{238}U. Note: the energy spectra for Pb and U in particular should be treated with caution (see text for details).

$$\frac{d\sigma^2}{d\Omega dE_p} = \frac{1}{4\pi}\frac{d\sigma}{dE_p}\frac{\eta}{\sinh(\eta)}\{\cosh(\eta\cos\theta) + f_{\mathrm{MSD}}\sinh(\eta\cos\theta)\}. \quad (4.1)$$

The slope η should, to first order, be a function of only a so-called energy parameter, which depends on the empirical binding energy of the emitted particle in the composite nucleus, the projectile binding energy and the total kinetic energy of the ejectile. We refer the reader to Refs. [21,22] for more precise formulation of this energy parameter. The angle integrated cross section $d\sigma/dE_p$ and the fraction f_{MSD} of the

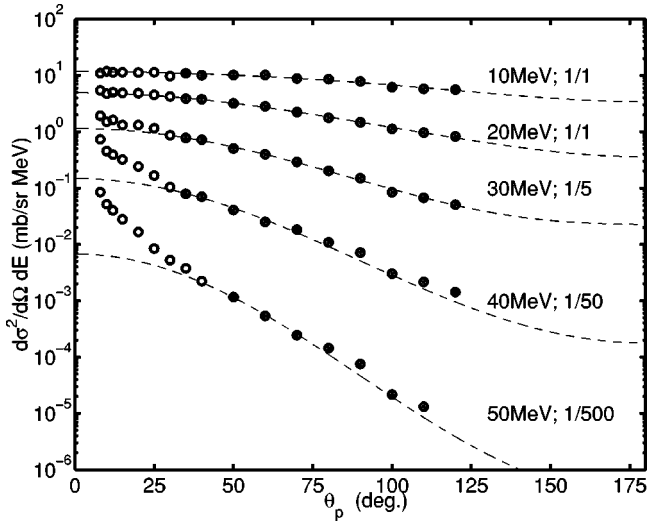

FIG. 4. Double differential angular distributions for various emission energies of protons from 100 MeV deuterons on ^{58}Ni in the laboratory frame. The measured data, represented by dots, are multiplied by the factors (indicated together with emission energies) for purposes of display. Dashed curves are the best fits based on Kalbach-Mann formulas [22] (see text for details).

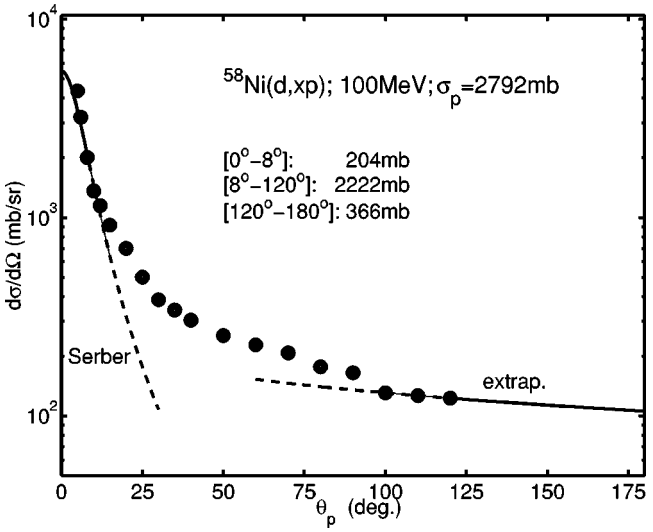

FIG. 5. Energy-integrated proton production cross section σ_p for the ^{58}Ni(d,xp) reaction at $E_d = 100$ MeV. Contributions from three different angular regions are given explicitly. Experimental data are given by the dots while the curves are extrapolations to smaller and larger angles, respectively (see text for details).

multistep direct reaction cross section are assumed to be known either from preequilibrium model calculations or from experiment [22].

Calculations performed with Eq. (4.1) were fitted to the experimental points represented by the shaded circles, which are assumed to originate largely from multistep processes as shown in Fig. 4. We found that the angular distributions for low-energy protons can be fitted without any difficulties at all angles (see dashed curves for 10 MeV and 20 MeV). However, as expected this phenomenological formulation fails to give a reasonable description of proton angular distributions for higher emission energies ($E_p > 30$ MeV) and at the very forward angles ($\theta_p < 40°$). Under these angular and energy conditions, the direct breakup of the incident deuteron dominates the proton production processes, which is not taken into account in the present KM formulation [22]. Nevertheless, the present use of the KM systematics in consistently describing the preequilibrium emission of the protons should be seen as a guideline in the understanding of the reaction mechanism in terms of multistep processes.

C. Integrated cross sections and multiplicities

In Fig. 5 the energy-integrated proton angular distribution of the ^{58}Ni(d,xp) reaction is presented. In order to estimate the angle-integrated cross sections in the angular region $\theta_p = [0°,8°]$, the Serber model for deuteron breakup [9] was employed, calculations of which are also shown in Fig. 5. Note that a standard minimization technique was used to renormalize the theoretical curve to the existing experimental points at the most forward angles where the Serber model seems to work well for $\theta_p < 15°$. In the angular region $\theta_p = [120°,180°]$ a standard extrapolation-interpolation method was employed to obtain those integration points which fall outside the experimental data (see Fig. 5). The overall error of the integrated proton production cross section σ_p is $\sim 10\%$ for all target nuclei, except for the uranium target as we have already discussed above.

In Fig. 6 we show the dependence of the total proton production cross section σ_p as a function of target mass. We find that σ_p reaches a maximum in the mass region around ^{58}Ni. The decrease in σ_p towards the heavy-mass nuclei undoubtedly reflects the increasing importance of neutron emission and fission, and because the increasing Coulomb barrier inhibits the emission of low-energy charged particles. We find that our data are in good agreement with the measurements reported by Wu *et al.* [17] for similar targets but at

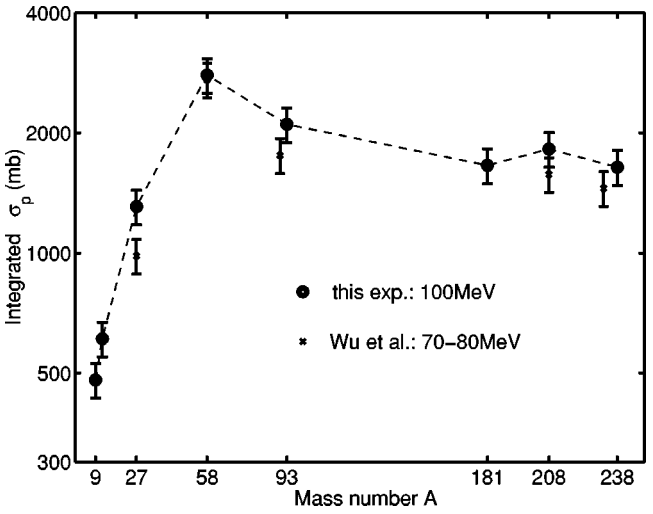

FIG. 6. The variation of the total proton production cross section σ_p with target nuclear mass A. In addition to the experimental data of this study (solid circles), the data of Wu *et al.* [17] (crosses) taken at lower deuteron energies are plotted for comparison. The dashed curve is to guide the eye. Note the log scales.

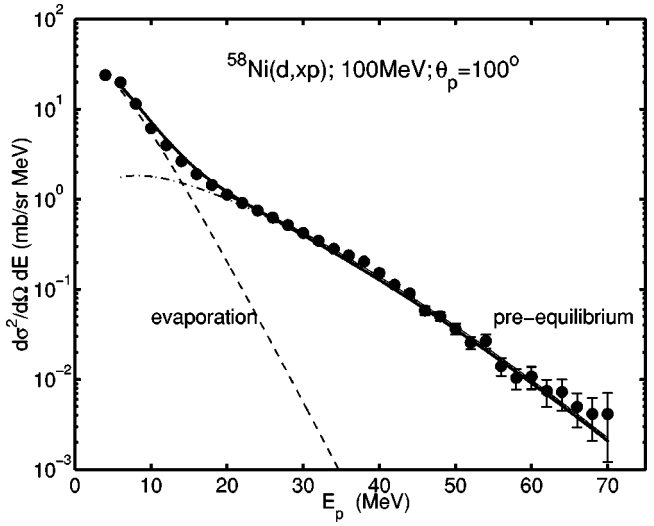

FIG. 7. A typical proton energy spectrum at a backward angle. The evaporation (dashed) and preequilibrium (dash-dotted) contributions are indicated separately. Their incoherent sum is represented by the solid line.

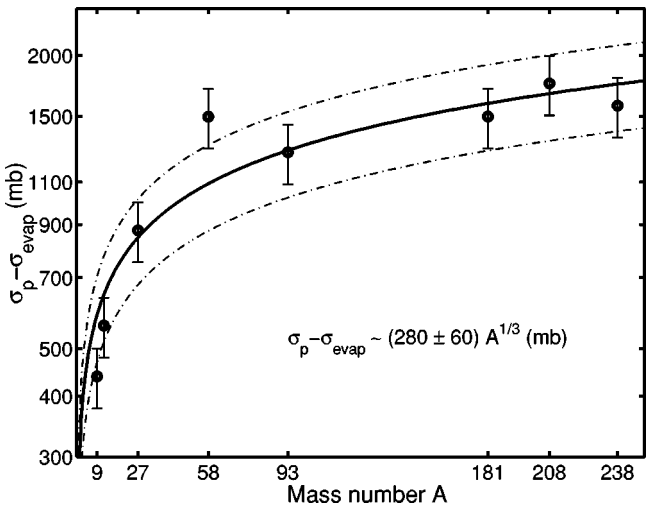

FIG. 8. The variation of preequilibrium proton cross section $(\sigma_p - \sigma_{\rm evap})$ with the target nuclear mass A. The solid thick line shows the $A^{1/3}$ dependence. Note the log scales.

lower incident deuteron energies as indicated in Fig. 6. However, the present values of the total cross section should be more accurate due to the new data measured at more forward angles.

As we have already mentioned, for angles larger than 90° the energy spectral shapes and the magnitudes of the evaporation peak are almost constant for a particular nucleus, indicating that the proton yield at the backward angles is dominated by the compound nuclear evaporation process. Figure 7 represents a typical energy spectrum of the back-scattered protons. Using the Weisskopf evaporation model [23], we fit the data points at the evaporation peak as shown by the dashed curve. It seems that at the backward angles a smaller but non-negligible preequilibrium component also appears to exist, which we take into account by fitting the experimental data with a simple Gaussian distribution (to simplify the numerical integration) given by the dashed-dotted curve. By adding the evaporation and preequilibrium contributions we reproduce the experimental data as shown by the solid line in Fig. 7. The same procedure was performed over all backward angles measured and, assuming that the angular distribution of the evaporation spectrum is symmetric about 90°, we obtain the integrated evaporation cross sections $\sigma_{\rm evap}$ for all target nuclei.

Figure 8 shows the total preequilibrium proton production cross section, which was obtained by subtracting the evaporation (equilibrium) contribution σ_{evap} from the total cross section σ_p (neglecting the relative small contributions from the discrete states). We find that the expression $(\sigma_p - \sigma_{\rm evap})/A^{1/3}$ remains constant as a function of the target mass A. The best fit to $(\sigma_p - \sigma_{\rm evap})$ using an $A^{1/3}$ dependence is presented in Fig. 8 by the solid curve. The production of energetic preequilibrium protons therefore appears to be proportional to the nuclear radius, suggesting that these protons may result mainly from peripheral collisions.

Proton (Y_p) multiplicities were extracted from the experimental data by using the expression $Y_p = \sigma_p / \sigma_R$. The reaction cross sections σ_R measured for incident deuterons on Be, Ni, and Pb (and a number of other targets) at 97.4 MeV were taken from Ref. [24]. Corresponding neutron multiplicities $Y_n = \sigma_n / \sigma_R$ were obtained from LAHET code system model calculations which are discussed in the next section. These multiplicities are shown in Fig. 9 for the Be, Ni, and Pb targets. It is found that the values of Y_p and Y_n behave oppositely to each other as a function of the target mass. At the target mass of Ni the total proton yield is at the maximum, while the total neutron yield is at a minimum. This can be explained in terms of the neutron evaporation and fission which become more favorable for heavier nuclei. For heavier nuclei also the Coulomb barrier attenuates the emission of

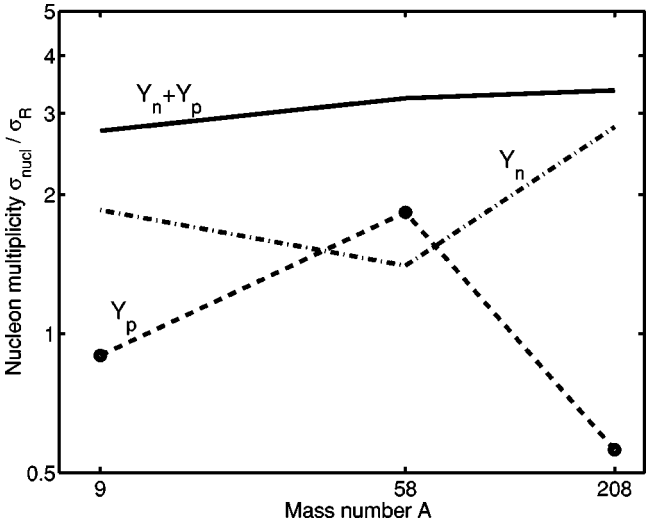

FIG. 9. Variation of the total mean proton (Y_p), neutron (Y_n), and nucleon $(Y_n + Y_p)$ multiplicities with the target nuclear mass A at $E_d = 100$ MeV. The two lines are merely guiding the eye. Note the log scales.

low-energy charged particles. On the other hand, it has already been shown that the $d+\mathrm{Be}$ reaction is very efficient in neutron production [10,20]. Therefore, it is not surprising that the corresponding proton production in the case of this light nucleus is rather suppressed.

We also show in Fig. 9 that the total nucleon multiplicity Y_n+Y_p is not so sensitive to the nuclear mass when compared to Y_n and Y_p separately. This suggests that the sum of the production yield of other charged particles (d, t, ^{3}He, and ^{4}He) is nearly constant as a function of target mass, perhaps slightly higher for lighter nuclear masses.

A brief summary of experimental results is presented in Table I. Coulomb barriers were obtained from $V_c = 1.44\,Z/1.5(A^{1/3}+1^{1/3})$ for different targets with mass A and charge Z. For those targets, where there were no experimental data available, the reaction cross sections were calculated from the best fit to the existing experimental data using the empirical expression $\sigma_R=\pi(1.58A^{1/3}+0.671\,A_d^{1/3})^2$ taken from Ref. [24]. Here A and A_d are target and deuteron mass numbers, respectively.

V. COMPARISON WITH THE LCS MODEL CALCULATIONS

The present experimental results are compared to theoretical predictions within the framework of the LAHET code system [12] [intranuclear cascade (INC) + evaporation (EVAP)]. The physics involved in the models of the LAHET code system (LCS) are discussed in detail in Ref. [12]. However, we note an important difference between the INC and EVAP underlying models: the INC calculations follow the history of individual nucleons in a classical or semiclassical manner leading to an equilibrated system, while the EVAP calculations follow the deexcitation of the whole nucleus when it decays statistically from one excitation level to another. The connection between these two approaches is currently one of the most delicate points of intermediate–to–high-energy simulations of nucleon-nucleus reactions. In general, the single particle approach of INC should be justified as long as nucleons can be treated classically, i.e., the wavelength λ of the incident nucleon is smaller than the nucleon radius. In other words, $\lambda<\pi/2$ fm and similarly $E>160$ MeV. On the other hand, the EVAP approach should be valid as long as the energy of the nucleon does not exceed the separation-plus-Fermi energy by about 40 MeV, i.e., when the thermal equilibrium of the system is reached. Beyond this point the standard evaporation is assumed. Thus, the transition energy between the INC and EVAP calculations cannot be specified rigorously. For this reason most of the high-energy codes, including the LCS, are still searching for a suitable extension of INC which is able to describe the entire preequilibrium part of the cross section in order to link both the INC and EVAP energy domains.

It should be mentioned that the INC/EVAP model was created for applications involving particle generators for which high-energy transport codes are required. Nevertheless, it has the advantages of energy and momentum, charge and baryon-number conservation even in the case of residual nuclei. Although it is questionable whether INC calculations are able to make accurate predictions for incident deuteron energies less than or equal to 100 MeV, certain features of the particle and isotope production can be understood, at least qualitatively, in terms of a prompt nuclear cascade followed by particle evaporation.

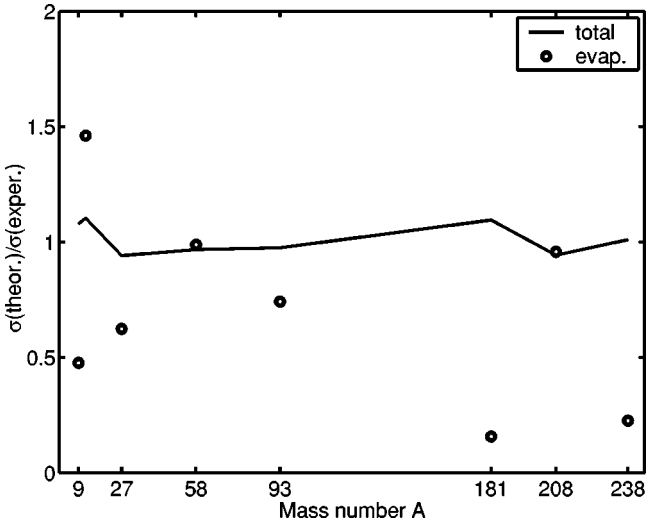

FIG. 10. The ratio σ_p(theoretical)/σ_p(experimental) for total proton production cross section with 100 MeV deuterons is presented as a function of the target mass number by the solid line. The corresponding ratios for proton production from the evaporation process are shown separately with the circles. See also Table I.

For the deuteron induced reactions within the LCS we employ the ISABEL INC model [6] coupled to the multistage preequilibrium exciton model (MPM) [25] followed by the evaporation model (EVAP) [26]. Three types of LCS calculations were performed and are labeled as follows.

(a) ''INC1'' is the ISABEL INC calculation, which takes into account the refraction of charged particles caused by both the Coulomb potential and the nuclear optical potential. The MPM contribution is included in this calculation.

(b) ''INC2'' is the ISABEL INC calculation, for which neither Coulomb interaction nor nuclear refraction is permitted. The MPM is included.

(c) ''INC3'' is a similar calculation as ''INC1,'' except that the MPM option is suppressed.

A. Integrated proton production cross sections

The LCS model using the INC1 option was employed to perform calculations of the total proton production cross sections for 100 MeV deuterons on all eight targets. These results are compared to the experimental values as ratios, i.e., σ_p(theoretical)/σ_p(experimental), as shown as solid curve in Fig. 10. The agreement between the experimental and theoretical values is surprisingly good and is within 10% for all targets. It is important to note that the use of an optional Coulomb and nuclear refraction of charged particles within the LCS is strongly recommended. When this refraction is omitted in the case of INC2, we obtain a systematic overestimation of the total proton production cross sections of $\sim$20%. The overestimation occurs in the angular region from 20° to 70° as will be discussed below.

In Fig. 10 we also plot separately the ratio of σ_p(theoretical)/σ_p(experimental), presented by circles, the proton production cross sections for the evaporation process. Good agreement is obtained only for Ni($A=58$) and Pb($A=208$) nuclei. In the case of the remaining targets, the model calculations present large discrepancies when compared to the values extracted from the experiment. This would suggest that the transition from the INC stage to the decay of an equilibrated compound nucleus is still treated somewhat arbitrarily within the LCS. Further theoretical work is awaited along these lines. On the other hand, for the nuclei, such as Be, C, Ta, Pb, and U, more than 90% of the secondary protons are produced through direct preequilibrium processes as shown in Table I. Therefore, despite the large discrepancies found in the prediction of the proton evaporation cross section the evaluated total integrated cross sections are consistent with the experimental data.

B. Energy spectra and angular distributions

In Fig. 11 we compare the experimental energy integrated proton production cross sections from 100 MeV deuterons on Be (upper part) and Pb (lower part) with various LCS predictions. It seems that the LCS calculation INC1 has no difficulties in reproducing the data over the full angular region in the case of the Be(d,xp) reaction. The suppression of the preequilibrium model viz. INC2 has no visible effect on such a light nucleus. However, the calculation with nuclear refraction is strongly recommended. INC3 overpredicts the experimental angular distribution in the region from 20° to 70° by roughly 20%. The Coulomb breakup term of the deuteron, given as thin solid line, leaving the target nucleus in its ground state, does not contribute to the angular distribution significantly.

In the case of heavy targets, e.g., ^{208}Pb, the contribution from the preequilibrium model is crucial in order to reproduce the data at backward angles ($\theta_p > 90°$). Here we compare INC1 with MPM and INC2 without MPM in the lower part of Fig. 11. The INC3 calculation, which does not take the refraction into account, is not recommended at all. It overpredicts the experimental angular distribution in the same region as the Be nucleus by about 25%. The backward angles are also clearly underestimated. Finally, we note that none of the standard LCS model calculations are able to reproduce the experimental spectra for heavy nuclei ($A>58$) at the very forward angles ($\theta_p \leqslant 12°$) of the emitted protons. As has already been suggested in [11], the Coulomb breakup of the deuteron, which we calculate independently, is not taken into account properly in the LCS modeling. Therefore, at the very forward angles and for heavy nuclei the angular distributions are underestimated by the LCS as shown in Fig. 11.

This is best illustrated in Fig. 12, where we compare the experimental and theoretical values of the double differential proton energy spectra for the Pb(d,xp) reaction at 10° (upper part) and 100° (lower part). The measured peak at $\theta_p = 10°$ is more than three times larger than the LCS INC1 calculation. The contribution of the Coulomb breakup process, represented by the dashed curve, added to the LCS curve brings the theory, shown as a solid line, very close to the experimental data. On the other hand, the Coulomb breakup term becomes negligible at the backward angles as can be seen in the lower part of the same figure. Here the pure LCS predictions expressed by the dash-dotted histogram give a reasonable description of the experimental data.

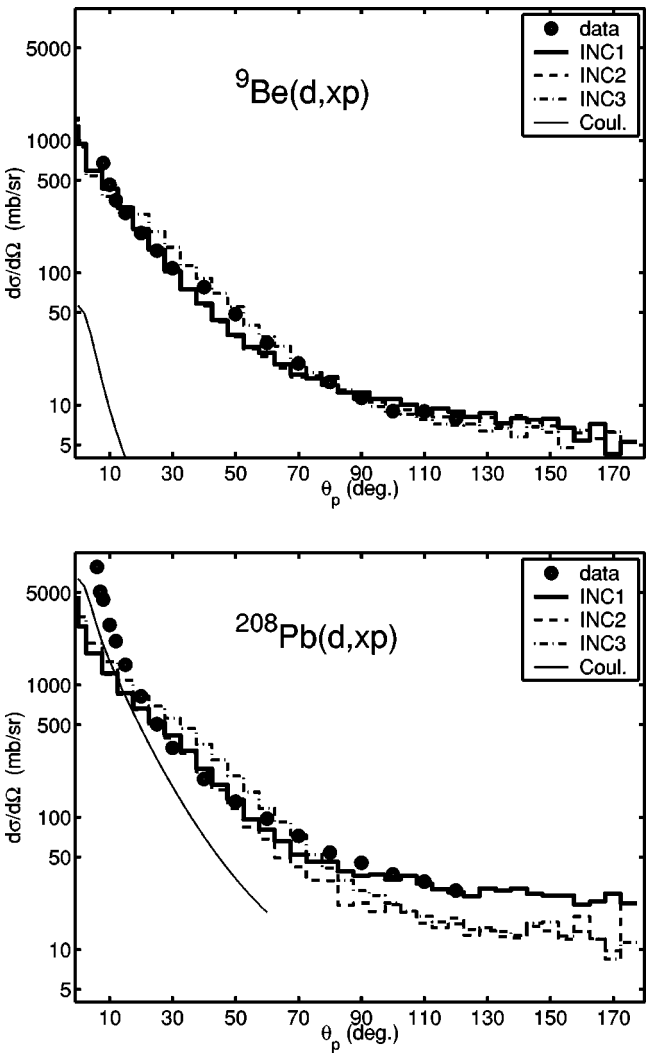

FIG. 11. The comparison of the experimental energy-integrated proton angular cross sections (data points) with the different LCS model calculations (INC1, INC2, INC3) for 100 MeV deuterons on ^{9}Be (upper part) and ^{208}Pb (lower part) in the laboratory frame. The contribution from the Coulomb breakup of the deuteron (Coul.) is plotted separately for comparison.

Similar to ^{208}Pb (Fig. 12), the double differential proton energy cross sections for the ^{9}Be(d,xp) reaction are plotted in Fig. 13. Here the ISABEL INC1 calculation seems to reproduce the data both in the absolute value and the position of the breakup peak. The broader theoretical energy spectrum of protons at $\theta_p = 10°$ (upper part) is not surprising. Such a light nucleus as Be hardly satisfies the statistical assumptions of the LCS physics models. The Coulomb breakup of the deuteron for light nuclei, such as Be or C, is negligible both at forward and backward angles.

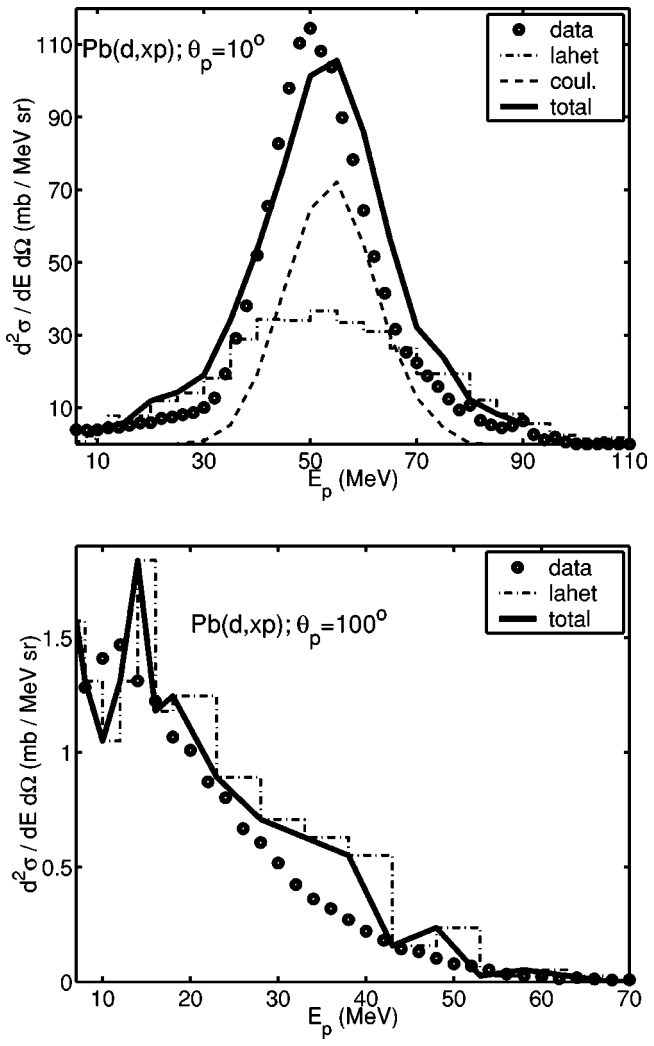

FIG. 12. The comparison of the experimental proton cross sections (data: points) for 100 MeV deuterons on ^{208}Pb at $\theta_p = 10°$ (upper part) and $\theta_p = 100°$ (lower part) in the laboratory frame with the pure LCS model calculations (dot-dashed). The Coulomb breakup of the deuteron (coul.) contributes only at forward angles, and is represented by dashed curve. Solid curve (total) is the sum of LCS and Coulomb terms.

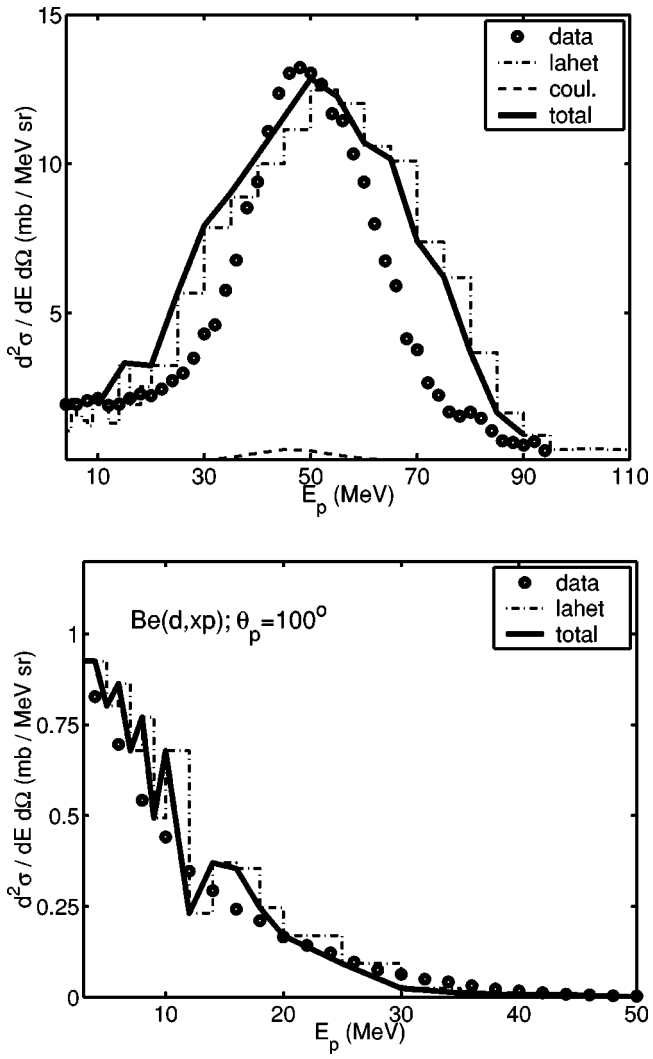

FIG. 13. Same as Fig. 12 but for 100 MeV deuterons on ^{9}Be.

VI. SUMMARY AND CONCLUSIONS

Double differential proton cross sections were measured in the bombardment of 100 MeV deuterons on Be, C, Al, Ni, Nb, Ta, Pb, and U. The emitted protons were detected by two- and three-counter telescopes using combinations of $\Delta E'$-E and ΔE-$\Delta E'$ techniques for particle identification. The experimental cross sections are accurate to within 10% in absolute value and with a low energy cutoff of a few MeV.

Existing angular distributions have been extended to much more forward angles, i.e., from 20° down to 8° for heavy nuclei and down to 6° for light nuclei, despite the considerable increase in background contributions experienced in these kind of measurements. Therefore, we conclude that standard two- and three-counter telescopes, using combinations of $\Delta E'$-E and ΔE-$\Delta E'$ techniques, can be employed for charged light particle measurements at the detection angles as close as 6°–8° with respect to the beam. We suggest that the extension of such measurements down to the very forward angles, say, $0 \leqslant \theta_p \leqslant 8°$ could be pursued by the means of a magnetic spectrometer [27].

The measured proton spectra from the eight target nuclei show surprisingly systematic behavior and considerable similarity. The most important features observed are the following.

(i) The deuteron breakup process dominates the proton spectra at forward angles, and the breakup contribution increases with increasing target mass.

(ii) The high-energy continuum of emitted protons decreases rapidly in magnitude with increasing angle. For medium mass nuclei, the low-energy region is dominated by an evaporation peak. A small non-negligible preequilibrium yield is also observed at backward angles, where the energy spectra are rather constant.

(iii) The evaporation process is comparable ($\sim$40%) to the preequilibrium process for medium mass nuclei, while preequilibrium processes dominate ($\sim$90%) the emission of protons for light and heavy nuclei.

(iv) The total proton yield reaches a maximum in the mass region around ^{58}Ni. The decrease in proton yield for heavier mass nuclei reflects the increasing importance of neutron emission and fission, as the increasing Coulomb barrier inhibits the emission of charged particles.

(v) The preequilibrium proton yield increases steadily with target mass and is roughly proportional to $A^{1/3}$.

Angular distributions of protons emitted into the continuum were used to also test the phenomenology of Kalbach-Mann over the angular and target-mass range of the present study. This phenomenology is able to qualitatively reproduce the proton emission spectra except for the regions at forward angles where the breakup of the incident deuteron dominates. Although no direct information on the breakup mechanism can be extracted, these systematics nevertheless can provide some guidance on the qualitative contributions of multistep direct and multistep compound processes to the reaction mechanism of preequilibrium proton emission.

The main objective of the present study was however to test and apply the existing LAHET code system (LCS) of the proton production at an incident deuteron energy of 100 MeV and over a wide target mass range. The present experimental data are compared to theoretical predictions within the framework of the LCS (intranuclear cascade + evaporation). All the integrated proton production cross sections are reproduced to within 10% for all targets examined. However, a few important findings, related to the energy spectra and angular distributions, are as follows.

(1) We confirm that the Coulomb breakup of the deuteron is not taken into account properly by the LCS. The LCS alone fails to reproduce the data at the very forward angles ($\theta_p < 12°$) in the case of heavy targets ($A \gtrsim 58$). The inclusion of the missing Coulomb breakup term brings the theory very close to the experimental results without any further renormalization.

(2) The inclusion of the refraction of charged particles due to both the Coulomb and nuclear potential improves the theoretical angular distributions of the emitted protons in the full angular region and for all targets when compared to the data.

(3) The use of the preequilibrium model is indispensable for the reproduction of the data at backward angles ($\theta_p > 90°$) both for medium and heavy mass targets.

(4) The transition from the INC stage to the decay of an equilibrated compound nucleus is still somewhat arbitrary within the application of the LCS. The LCS fails to reproduce the evaporation contribution extracted from the experiment. Therefore, further improvements of the LCS physics models are essential along these lines.

In this study standard codes commonly used in the analyses of proton-induced reactions at medium energies (0.8–1.6 GeV) on heavy targets were implemented successfully to extract information on the different mechanisms contributing to the measured proton cross sections in deuteron-induced reactions at an incident energy of 100 MeV. With regard to the part of the cross sections dominated by the breakup of the incident deuteron, this study emphasizes the importance of including the Coulomb breakup term of the deuteron in the present calculations. Hence, the present results are able to assist in the theoretical application of the model to describe and predict proton production in deuteron-induced reactions at an incident energy as low as 100 MeV. These results should provide useful guidelines for similar studies of differential neutron and proton production cross sections also at higher deuteron energies.

ACKNOWLEDGMENTS

We would like to express our thanks to the NAC cyclotron crew for delivering the high quality deuteron beam. The authors are also grateful to J.A. Tostevin and Y. Yariv for helpful discussions. Finally, we wish to express our appreciation to R.E. Prael for providing us with the LAHET code system.

[1] C.D. Bowman *et al.*, Nucl. Instrum. Methods Phys. Res. A **320**, 336 (1992).

[2] Spallation Neutron Source (SNS) Status Report, 1999, ORNL, USA, URL http://www.ornl.gov/sns/

[3] European Spallation Source (ESS) — a Next Generation Neutron Source for Europe, EU, 1999, URL http://www.isis.rl.ac.uk/ESS/

[4] H. Nifenecker, S. David, J.M. Loiseaux, and A. Giorni, Institut des Sciences Nucléaires de Grenoble Report No. ISN 99.04, 1999.

[5] H.W. Bertini, Phys. Rev. **188**, 1711 (1969); **131**, 1801 (1963).

[6] Y. Yariv and Z. Fraenkel, Phys. Rev. C **20**, 2227 (1979).

[7] J. Cugnon, C. Volant, and S. Vuillier, Nucl. Phys. **A625**, 729 (1997); J. Cugnon, *ibid.* **A462**, 751 (1987).

[8] R. Serber, Phys. Rev. **72**, 1114 (1947).

[9] R. Serber, Phys. Rev. **72**, 1008 (1947).

[10] D. Ridikas and W. Mittig, Nucl. Instrum. Methods Phys. Res. A **418**, 449 (1998); D. Ridikas and W. Mittig, *Proceedings of the 3rd International Conference on Accelerator Driven Transmutation Technologies (ADTT'99)*, Praha, Czech Republic, 1999, Proceedings ADTTA'99, URL http://www.fjfi.cvut.cz/con_adtt99/

[11] D. Ridikas, W. Mittig, and J.A. Tostevin, Phys. Rev. C **59**, 1555 (1999).

[12] R.E. Prael and H. Lichtenstein, ''User Guide to the LCS: the LAHET Code System,'' Los Alamos National Laboratory Report No. LA-UR-89-3014, 1989.

[13] O. Bersillon, ''TIERCE Code System,'' *Proceedings of 2nd International Conference on Accelerator Driven Transmutation Technologies*, Kalmar, Sweden, 1996, edited by H. Condé (Uppsala University Press, Uppsala, 1997).

[14] D. Ridikas, Ph.D. thesis, GANIL Report No. GANIL T-99-04, available by request from GANIL, BP5027, F-14076 Caen Cedex 5, France.

[15] E. Martinez, Ph.D. thesis, available by request from DPTA/SPN, Commissariat à l'Energie Atomique (CEA), F-91680

Bruyères-le-Châtel, France; E. Martinez *et al.*, Nucl. Instrum. Methods Phys. Res. A **385**, 345 (1997).
[16] J.A. Tostevin *et al.*, Phys. Lett. B **424**, 219 (1998); J.A. Tostevin, S. Rugmai, and R.C. Johnson, Phys. Rev. C **57**, 3225 (1998).
[17] J.R. Wu, C.C. Chang, and H.D. Holmgren, Phys. Rev. C **19**, 370 (1979).
[18] A.H. Botha and H.N. Jungwirth, in *Proceedings of the 10th International Conference on Cyclotrons and Their Applications*, Michigan, 1984, edited by F. Marti (IEEE, New York 1984), p. 263.
[19] J.V. Pilcher *et al.*, Phys. Rev. C **40**, 1937 (1989).
[20] D. Ridikas and W. Mittig, Heavy Ion Phys. **10**, 51 (1999); in *Proceedings of the 2nd International Conference on Exotic Nuclei and Atomic Masses (ENAM'98)*, Michigan, 1998, edited by B. M. Sherrill, D. Morrissey, and C. N. Davids, AIP Conf. Proc. No. 455 (AIP, New York, 1998), p. 1003.
[21] C. Kalbach and F.M. Mann, Phys. Rev. C **23**, 112 (1981); C. Kalbach, *ibid.* **23**, 124 (1981).
[22] C. Kalbach, Phys. Rev. C **37**, 2350 (1988).
[23] V. Weisskopf, Phys. Rev. **52**, 295 (1937).
[24] A. Auce *et al.*, Phys. Rev. B **348**, 697 (1996).
[25] R.E. Prael and M. Bozoian, Report No. LA-UR-88-3238, Los Alamos National Laboratory, 1988.
[26] L. Dresner, ''EVAP—A FORTRAN Program for Calculating the Evaporation of Various Particles from Excited Compound Nuclei,'' Report No. ORNL-TM-196, Oak Ridge National Laboratory, 1962.
[27] H. Okamura *et al.*, Phys. Lett. B **325**, 308 (1994); H. Okamura *et al.*, Phys. Rev. C **58**, 2180 (1998).